Simultaneous emergence of active turbulence and odd viscosity in a colloidal chiral active system

Joscha Mecke
Forschungszentrum Juelich https://orcid.org/0000-0001-8984-6990
Yongxiang Gao
Shenzhen University https://orcid.org/0000-0003-4042-0248
Carlos Ramírez-Medina
Forschungszentrum Juelich
Dirk Aarts
University of Oxford https://orcid.org/0000-0001-8333-015X
Gerhard Gompper
Forschungszentrum Jülich https://orcid.org/0000-0002-8904-0986
Marisol Ripoll (m.ripoll@fz-juelich.de)
Forschungszentrum Juelich https://orcid.org/0000-0001-9583-067X

Article

Keywords:

Posted Date: September 28th, 2022

DOI: https://doi.org/10.21203/rs.3.rs-2072915/v1

Simultaneous emergence of active turbulence and odd viscosity in a colloidal chiral active system

J. Mecke*[1], Y. Gao*†[2], C.A. Ramirez-Medina[1], D.G.A.L. Aarts[3], G. Gompper[1], and M. Ripoll‡[1]

[1]Institute of Biological Information Processing, , Forschungszentrum Jülich, 52425 Jülich, Germany

[2]Institute for Advanced Study, Shenzhen University, Shenzhen, China

[3]Department of Chemistry, Physical and Theoretical Chemistry Laboratory, , University of Oxford, Oxford, United Kingdom

September 16, 2022

Abstract

The simultaneous emergence of active turbulence and odd viscosity for a colloidal rotors system is here shown. Rod-like colloidal particles with a ferromagnetic head and magnetic moment perpendicular to the rod axis, precess vertically to the substrate under an externally rotating field. The colloid rotation drags the adjacent fluid inducing the translation of neighbouring colloids, behaviour which is also captured by hydrodynamic simulations of discs rotating in sync. Experiments and simulations reveal that multi-scale eddies emerge with an energy spectrum following a power-law decay: this feature of self-similar dynamics without the emergence of a dominant vortex size is characteristic of active turbulence. Moreover, the particles are dragged to the center of the vortices, a telltale sign of systems with odd viscosity, which is explicitly measured. Our findings are relevant for the understanding of biological systems and for the design of microrobots with collective self-organized behavior.

Active matter consists of agents, which include one or more building blocks that can convert energy into forces or torques, or are externally driven, leading to an inherent motion.[1,2] The interactions among the individual active units can largely vary making the different systems exhibit extensive number of structures, together with the emergence of a broad range of collective motions. These phenomena can be found across a wide range of length scales, *e.g.*, in flocks of bird,[3] traffic dynamics,[4] swarming in bacterial colonies,[5,6] or cluster, swarm and lane formation in self-phoretic colloids.[7,8] Understanding the nonequilibrium physics of active matter is of major importance in unravelling the processes of life, since all living biological systems are driven far from equilibrium.

Active micrometer-scaled particles powered by externally imposed electro-magnetic manipulation serve as a promising candidate for designing agents capable of applications such as nanomedical drug delivery.[9–11] A prominent example is given by particles carrying a magnetic moment exposed to externally applied magnetic fields,[9,12–17] which can be used to steer tracer particles through a solvent,[9] or be brought into a rotating state by imposed torques[12–18] becoming then an archetypical synthetic chiral active fluid. Biological examples of chiral active fluids are membranes with rotating macromolecules,[19] or *Volvox* colonies which have shown to hydrodynamically interact and organise in bound states of co-rotation.[20] These chiral systems show intrinsic density inhomegeneities, which can be related to the presence of an additional term in the system stresses that is odd under mirror or time-reversal symmetry:[21–23] this indicates the presence of the so-called odd viscosity. In soft matter chiral active systems, odd viscosity effects have so far only sparsely been realised experimentally.[24]

Active or mesoscale turbulence denotes a collective, chaotic motion emerging in bacterial suspensions,[25,26] swarming sperm,[27] or active nematics,[28–30] which is reminiscent of classical high-Reynolds number turbulence.[31] In classical turbulence, the Reynolds number is large and the only important length scales are provided by the energy dissipation scale and system size (energy cascade), or the energy injection scale and system size (inverse energy cascade). Between these two scales, the dynamics is behaving self-similarly, characterised by a power-law decay in the energy spectrum. In bacterial turbulence, the Reynolds number is small and the particle size is comparable with the energy injection scale. The competition between hydrodynamics, alignment, activity, and rotational diffusion introduce an additional relevant length scale in the dynamics,[32] such that the self-similar dynamics is thus only expected on length scales between the energy injection and a dominant length scale of the collective, chaotic eddies (typically the size of ten activated units),[31] often resulting into power-law decay in the energy spectrum of less than a decade. On the other hand, rotor systems have been shown to exhibit active turbulence without the emergence of a dominant length scale resulting in a power-law decay in the energy spectrum without intrinsic cutoff.[13,33] Interestingly, rotor systems have shown to either exhibit active turbulence, or to have an odd viscosity:[24,34] whether both features may occur simultaneously is still an open question, answered affirmatively in this paper.

Here, we report an experimental and numerical study of ensembles of rotating colloidal rods interacting only

*Contributed equally

†yongxiang.gao@szu.edu.cn

‡m.ripoll@fz-juelich.de

via hydrodynamic interactions, where both the odd viscosity and turbulence can be simultaneously observed and quantified. The rotors are silica rod-like colloids with a magnetic tip at one end, with the direction of the magnetic moment perpendicular to the rod axis (see the Methods section). The sedimented rotors follow an externally applied magnetic field almost instantaneously, and in a particular frequency range, they precess perpendicular to the container basis, resulting in an ensemble of synchronously rotating cylinders with parallel symmetry axes. In parallel, we conduct large-scale simulations with a model of discs rotating at a fixed angular velocity Ω, immersed in an explicit hydrodynamic solvent, and interacting with other discs by steric interactions[35–37] (see the Methods section). This assumes that the relevant interactions between the rotating rods take place only perpendicularly to their cylinder axes. The fluid in contact with the colloids surface co-rotates with it, generating long-range interactions between rotors, which induce the rotors' propulsion. This leads to similar ensemble dynamics and rich cooperative effects, such as dynamic vortex formation and mesoscale turbulence, all of which is a function of the packing fraction. The emergence of clear density-vorticity correlations allows us to reliably measure the odd viscosity of the system, which we expect to become a standard method of quantification in many chiral active systems. The persistent formation of vortices with sizes ranging from a few particle diameters to almost the whole system size results in a decay of the energy spectrum with a power-law of approximately a decade in experiments, and significantly larger in simulations, enabling us to demonstrate the self-similar dynamics.

In the remainder of the paper, we (i) introduce the dynamics of two interacting rotors, (ii) study the translational propulsion of rotors in dilute to dense ensembles, (iii) characterize the vorticity and density fields, which provides a measurement of the system's odd viscosity, and (iv) evaluate the active turbulence via the energy spectra.

I. Results

(i) Hydrodynamics of rotors pairs. The characterization of the dynamics of two rotors allows a first quantification of the relevant interactions in the system. Trajectories of two interacting rotors are shown in Figs. 1**a-d** for a duration of $\Omega t = 30$, which corresponds to $t = 3$s in experiments. When two rotors approach, they perform an orbital rotation around their joint centre of mass. This orbital rotation is fast at short separations, as can be seen in the trajectories shown in Fig. 1**a** and **c**, and slows down with increasing distance (Fig. 1**b** and **d**), becoming Brownian and independent of each other for even larger separations. The rotors are advected by the mutual flow generated, as shown in Fig. 1**e**, which is weaker for increasing distances. The angular velocity of the pair Ω_{pair} around their centre of mass is quantified from the measured trajectories and presented in Fig. 1**f**, where the decay as a function of the separation between the rotors is also evident. For one isolated rotor, the radial velocity profile can be estimated as $u_\varphi(r) = (\sigma/2)^2\Omega/r$, and for two, the position dependent flow field can be calculated as a superposition of the individual flow fields, yielding to a prediction of the angular velocity $\Omega_{\text{pair}}/\Omega = \sigma^2/(2r^2)$, where the boundary conditions on the surface of the rotors are disregarded. This quantitative prediction is in almost perfect agreement with the simulation measurements as can be seen in Fig. 1**f**: the analytical expression for the flow follows from the infinite cylinder approximation, which is valid for the 2D simulations. The experimental values are in qualitative agreement with these results, although systematically lower by approximately a factor two. The sedimented magnetic rods in experiments rotate in a container of height much larger than the rod length, such that the induced flow partially escapes into the upper fluid layers above the rods. Furthermore, the friction between the solvent and the substrate implies a no-slip boundary condition between fluid and substrate which diminishes the effective flow experienced by nearby rotors. Both effects are more pronounced at larger interparticle distances. the overall agreement between experiments and simulations, however, is very good, especially at short distances, where pair interactions are substantially stronger than the thermal noise.

The precise hydrodynamic force acting on a rotor due to the presence of a neighbour, as illustrated in Fig. 1e, can be explicitly measured in simulations by placing pairs of rotors at fixed positions and quantifying $F_\perp$ (indicated in Fig. 1**g**) as a function of their centres separation r. The thrust force $F_\perp$ acts on both rotors in the direction perpendicular to the line of centres, and is responsible for the pair orbital rotation. The results shown in Fig. 1**g** are normalized with F_s which assumes the Stokes drag of the colloid, *i.e.*, $F_s = \zeta v_s$, with the solvent friction $\zeta = k_{\text{B}}T/D$, obtained from the diffusion coefficient D of isolated rotors and the ambient thermal energy $k_{\text{B}}T$, and the velocity imposed at the colloid surface $v_s = \pi\sigma\Omega$, such that $F_s = 4\pi^2\eta\sigma\Omega$. Simulation measurements are compared in Fig. 1**g** with the calculation for infinitely long cylinders in a fluid of vanishing Re,[38] resulting in excellent agreement. It is hard to measure this thrust force directly in experiments, but it can be estimated by assuming the Stokes drag, using the velocity from the measured pair angular frequency in Fig. 1**f**, $v_\perp \simeq \pi\Omega_{\text{pair}}r$, and the solvent friction. This approach is considered for both experimental and simulated values of Ω_{pair} in Fig. 1**g**, which shows that using the Stokes drag provides a reasonable agreement at distances $r \gtrsim 3$. Interestingly, the decrease of $F_\perp$ with r indicates that the thrust force is significant over a long range, since it decays to the strength of thermal fluctuations $F_{\text{th}} = k_{\text{B}}T/\sigma$ only around $r \approx 10\sigma$, since $F_{\text{th}}/F_s \approx 0.01$ in our case.

(ii) Conversion of rotation into propulsion. The motion of more than two interacting rotors is now investigated as a function of the packing fraction ϕ. Rotor configu-

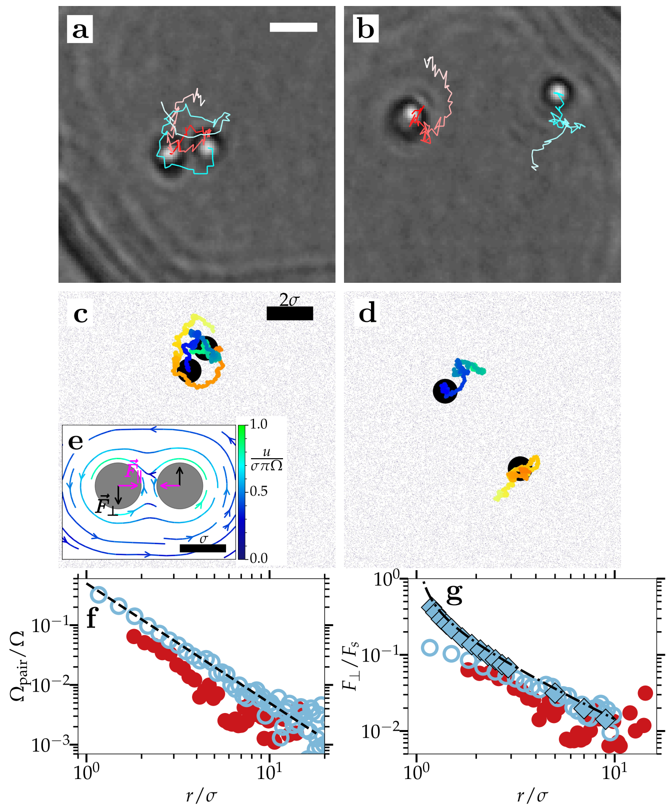

Figure 1: Hydrodynamic pair interactions. a-d. Trajectories of two interacting colloidal rotors at various separations, with lines color coding time evolution, and scale bars 2μm in experiments and 2σ in simulations (see related Movie); **a-b.** experimental trajectories for a duration of $\Omega t = 30$, where $t = 3s$, **c-d.** simulated trajectories with $\Omega t = 5$, with blue background points illustrating solvent positions. **e.** Flow field of two colloids placed at a fixed distance, as calculated from hydrodynamic simulations. **f.** Co-rotation angular velocity Ω_{pair} as a function of the separation of the two rotors: red, experimental results; blue, simulations. Dashed line is the theoretical prediction $\Omega_{\text{pair}}/\Omega = \sigma^2/(2r^2)$. **g.** Forces perpendicular to the line connecting two rotors in units of $F_s = 4\pi^2\eta\sigma\Omega$, with $F_s \simeq 0.01(k_BT/\sigma)$. Dashed-dotted line is the analytical prediction from the Stokes equation in Ref.,[38] blue squares correspond to the explicitly measured forces in simulations, and circles are estimates obtained from the angular velocity in **f** via $F_\perp = (k_BT/D)\pi\sigma\Omega$.

rations and typical trajectories are shown in Figs. 2**a-c** for experiments and in Figs. 2**d-i** for simulation results. In simulations, trajectories are easy to track and all are marked in grey, while experimentally, due to the limited frame rate of the image acquisition, full trajectories of all particles cannot be automatically tracked, such that typically 15-30 rotors are tracked, with a few representative ones shown in Figs. 2**a-c** (see related Movies). At low ϕ, rotors are far from each other, displaying merely Brownian motion, as can be seen in Figs. 2**a** and **d**. At medium densities, rotors are more likely to interact in pairs, triplets, or larger ensembles, and the trajectories become ballistic and curved, reminiscent of active Brownian particles (Figs. 2**b** and **e**). Two neighbouring colloids rotate around each other in the same angular direction as the intrinsic rotation. When additional rotors get in their proximity, they get incorporated into the same motion nucleating a rotating group, or *vortex*. These vortices grow in size until they start to interact with neighbouring vortices. The ensemble exhibits therefore a rich vortex dynamics where the rotating groups coalesce or break up dynamically, and individual rotors vividly interchange between different rotating groups. Although all colloids are spinning in sync with the external magnetic field, the resulting vortices rotate at different speeds, and they can eventually rotate in opposite direction when they need to adjust to the boundary conditions imposed by neighbouring vortices. The curvature of the trajectories shown in Figs. 2**b** and **e** depend on the configuration of nearby rotors, *i.e.*, on the size of the rotating group the respective rotor belongs to. Small groups lead to strongly curved trajectories, whereas larger groups lead to almost straight trajectories. Curiously, a few experimental and simulated trajectories show a looping behaviour, resulting from the change of orbiting motion of one rotor from one to a different partner, triplet, or small group. For larger densities, the phenomenology is basically the same, but trajectories are on average longer and some of them might even exhibit segments bending into different directions, which occurs when rotors change from one vortex to another. Figures 2**c** and **f** show the system at highest experimental trackable $\phi(= 0.14)$, and Figs. 2**g** - **i**, correspond to full simulation domains where the ensemble dynamics of multi-scale vortex formation is more obvious.

Each individual rotor is propelled through the system with a instantaneous linear and rotational velocity, which depends on the local rotor configuration. On average the motion can be mapped to that of active Brownian particles, and the averaged mean squared displacement (MSD) shows the three expected regimes: purely thermal diffusion at very short times, actuated at intermediate times, and enhanced diffusion at long times. The rotational diffusion is related here to the change of direction of the motion instead of to the change of to orientation of the rotor axis. Experimental and simulation results are shown in Fig. 2**j** for several available packing fractions. The measured MSD for each fixed ϕ are then fitted to that of an active Brownian particle[39] which provides well-defined values for the actuated velocity v_a and the rotational time τ_r both in experiments and in simulations, as summarized in Figs. 2**k** and 2**l**. At low ϕ, the rotors barely interact with others, and in the limit of $\phi \to 0$, there is no propulsion on average. In fact, at very low densities, the experimental MSD barely shows active behaviour, rendering a reasonable fit impossible. This is remarkably different to ordinary active Brownian particles, which at low ϕ exhibit an active gas phase[40] due to their inherent propulsion. With increasing density, the interactions between rotors become more frequent such that the active velocity first grows with ϕ. Upon further increase of the rotor density, the motion is increasingly restricted by steric interactions, and the effective fluid viscosity experienced by the rotors also grows, which even-

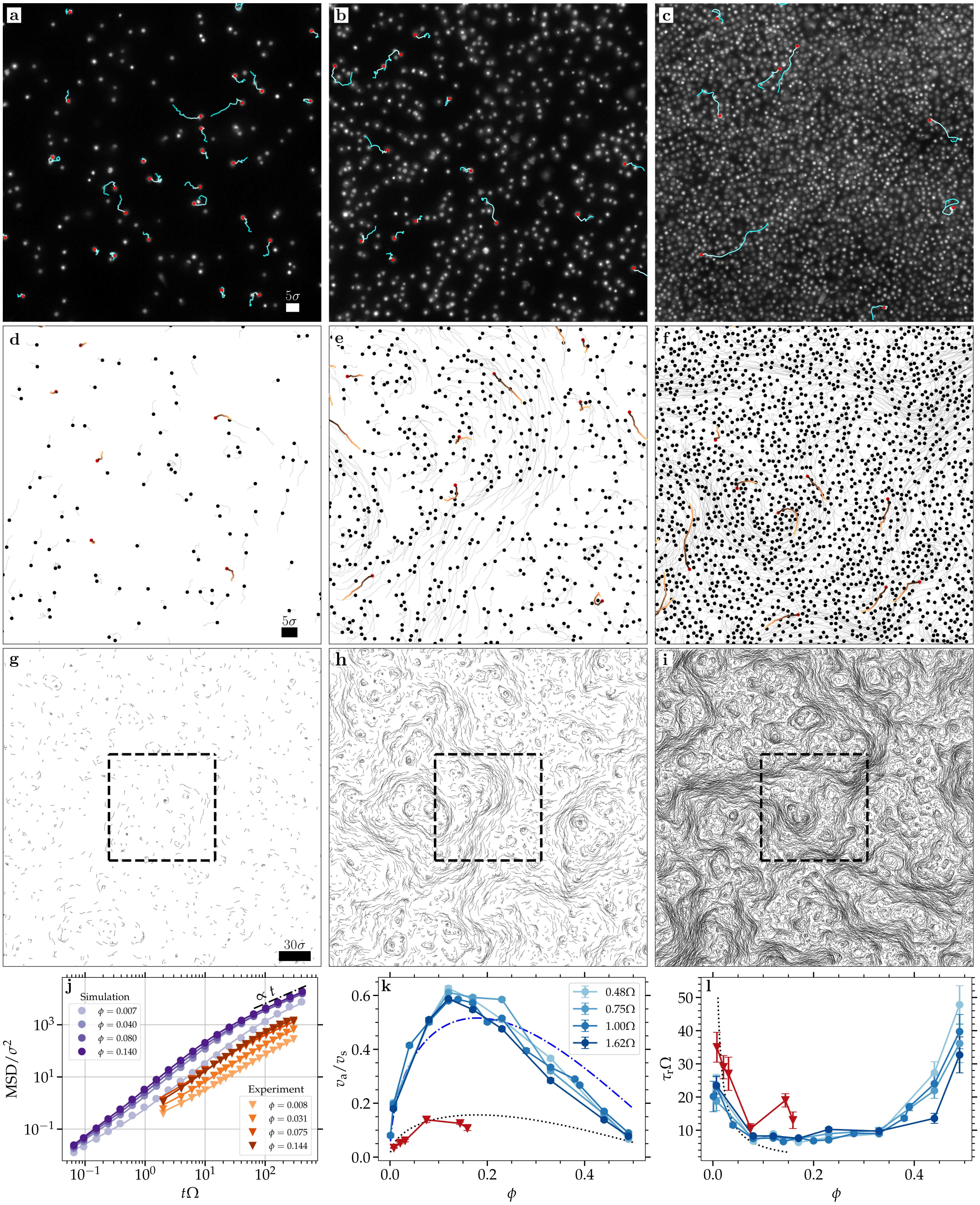

Figure 2: Collective dynamics of hydrodynamically interacting rotors. **a** - **c** *Fluorescent optical images of rotors at* $\phi = 0.008, 0.031$ *and* 0.144 *with an overlay of a few typical trajectories. Here, only a quarter of the full probe chamber is shown (see related Movies).* **d** - **f** *Simulated rotors configurations at* $\phi = 0.007, 0.04$ *and* 0.14 *with all trajectories in grey and few highlighted ones for comparison with experimental images. Trajectories are all drawn for a time* $\Omega t = 6$*. Only a part of the full simulation domain is shown.* **g** - **h** *Full simulation domains with trajectories, showing the formation of multiscale vortices. Dashed inset frames indicate the domains in* **d** - **f**. **j** *Mean-square displacements for experiments (orange triangles) and simulations (purple bullets) at different packing fractions in a square simulation box of length* $L = 100\sigma$ *with periodic boundary conditions. The lines correspond to respective least square fits to the active Brownian particle mean-square displacement.* **k** - **l** *Normalized active velocity* v_a*, and rotational diffusion time* τ_r *corresponding to the fits in* **j**. *Dotted (black) lines correspond to the analytical prediction* $v_a \simeq \pi\Omega\sigma(1-\phi/\phi_{\rm cp})^{2\phi_{\rm cp}}\sqrt{\phi/\pi}$*; dash-dotted line take into account an additional multiplicative fit factor of* 3.3.

tually completely impedes their motion. These trends qualitatively explain the maximum of v_a at intermediate values of ϕ seen in Fig. 2**k** for both simulations and experiments. In order to provide a quantitative estimate of this dependence,[41] we assume first that the thrust velocity $v_\perp$ of a rotor is simply due to pair interactions $v_\perp \simeq \pi\Omega_{\rm pair}\bar{r}$, as shown in Fig. 1**f**, and secondly, that the average distance between the rotors is that of a homogeneous system $\bar{r} \simeq (\sigma/2)\sqrt{\pi/\phi}$, such that $v_\perp \simeq (\pi\sigma\Omega)\sqrt{\phi/\pi}$. Simultaneously, the rotors dissipate momentum via mutual interactions and rotor density increases the effective fluid viscosity experienced by the rotors[42] which results in a decrease of the velocity at high density, as expected also for active Brownian particles.[43] The increase in viscosity for a 2D system of passive colloidal particles in linear order[44] is $\eta(\phi)/\eta_0 = 1 + 2\phi$, although in order to account for the abrupt increase when approaching the close packing density $\phi_{\rm cp}$, it is more appropriate to consider the phenomenological equation $\eta(\phi)/\eta_0 \simeq (1-\phi/\phi_{\rm cp})^{-2\phi_{\rm cp}}$.[45] The drag force considered for the thrust velocity $F_\perp \propto \eta_0 v_\perp$ can then be considered to balance with the drag of the effective velocity in a dense system $F_{\rm a} \propto \eta(\phi)v_{\rm a}$ which provides a full estimate of the effective active velocity $v_{\rm a} \simeq \eta_0/\eta(\phi)\, v_\perp$ in the full density range, as shown in Fig. 2**k.** This estimate agrees qualitatively very well with the simulation results, and perhaps somewhat surprisingly even quantitatively with the experimental measurements.

The measured $\tau_{\rm r}$ obtained from the MSD in Fig. 2**j** and shown in Figs. 2**l** corresponds to a rotational diffusion time only in the dilute limit. At larger densities, this time is related with rotational diffusion but also with an intrinsic rotation or change of direction, due the orbital motion in the vortices. To estimate $\tau_{\rm r}$, we consider the average time a rotor orbits another rotor before moving into a different orbit. In the regime of small densities, this time decreases with density; at intermediate densities, the presence of vortices of multiple sizes leads on average to $\tau_{\rm r}$ remaining constant, while for very high densities, where the rotors are basically not moving, $\tau_{\rm r}$ rapidly increases. In the limit of small densities, the time can then be approximated as $\tau_{\rm r} \simeq \bar{r}/v_\perp \simeq 1/(2\Omega\phi)$. This estimate works for both experiments and simulations, even at medium densities, as shown in Fig. 2**l.**

(iii) Vorticity and density fields: odd viscosity. With the ensemble configurations in Fig. 2 and the related velocity fields, the corresponding coarse-grained vorticity $\omega = \partial_x v_y - \partial_y v_x$ and local density ϕ_{loc} fields can be computed, as shown in Fig. 3. Areas with positive vorticity correspond to underlying vortices rotating in the same direction as the imposed magnetic field, areas with negative vorticity appear for vortices rotating in the opposite direction, which essentially fill the space in between the positive vorticity areas. Although qualitatively similar, the vorticity field measured in experiments is weaker than in simulations, due to the friction with the substrate.

The corresponding density fields in Fig. 3 also show clear inhomogeneities. Positive vorticity areas tend to be more populated than negative vorticity areas, both for experiments and simulations. This accumulation indicates the presence of a radial pressure on the rotating vortex originating from a non-vanishing *odd vicosity*.[22,46] As a first quantification of this effect, the probability density distribution is calculated separately for areas of positive and negative vorticity, displaying that both distributions are clearly displaced relative to each other, as shown in Fig. 4a. For positive vorticity, the maximum of the distribution occurs for densities larger than the average density, and conversely for negative vorticity. This means that areas with $\omega > 0$ tend to attract particles, and that they are depleted from $\omega < 0$ areas. The separation of the maximum of the distribution for a given density is larger for the lower average density in the investigated cases, which also show a broader distribution, and the trend can be clearly seen both in experiments and simulations.

In order to provide a quantitative characterisation of the odd viscosity, at a coarse-grained level, the rotors can be described using the continuum theory for chiral active fluids. Then, for an incompressible fluid, the vorticity spreads diffusively, and the related stresses are compensated by the pressure. However, if the system permits weak density inhomogeneities, the stresses due to a non-vanishing odd viscosity point to the centre of circulation, which translates (see Methods section) into an increase of the density linearly proportional to the given vorticity as,[22]

$$\frac{\Delta\rho}{\rho} = \nu^{\rm odd}\frac{\omega}{c^2}\,. \tag{1}$$

This expression is also valid when the vorticity ω is locally varying, such that $\Delta\rho = \rho(\boldsymbol{r}) - \langle\rho(\boldsymbol{r})\rangle$ is the local density change with respect to the average density in the system, with c the speed of sound, and $\nu^{\rm odd}$ the kinematic odd-viscosity, *i.e.*, the momentum diffusivity due to the presence of the odd stresses. Therefore, a circular flow of vorticity $\omega > 0$ is experiencing stress forces pointing to the centre of circulation, leading to rotor accumulation in the centre of the circular flow.[22] Similarly, a circular flow $\omega < 0$ leads to rotor depletion in the centre of circulation. The advantage of Eq. 1 is that it can be directly employed to quantify the system's odd viscosity. From data such as in Fig. 3, a histogram relating local vorticities and local densities can be evaluated, both in experiment and in simulation. The results presented in Fig. 4b show a linear dependence between local density changes and vorticity in the simulations as well as in the experiments. Fitting the lines in Fig. 4b with Eq. 1 allows then the accurate quantification of $\nu^{\rm odd}$ at different densities in the system, with resulting values shown in the inset of Fig. 4b. Interestingly, the experimentally measured odd viscosity is in reasonable agreement with the numerical results, which reflects that in both systems the two dimensional hydrodynamic rotation is responsible for the propagation of the stresses. In the investigated density range, $\nu^{\rm odd}$ decreases with density, due to the decrease of the compressibility of the system with increas-

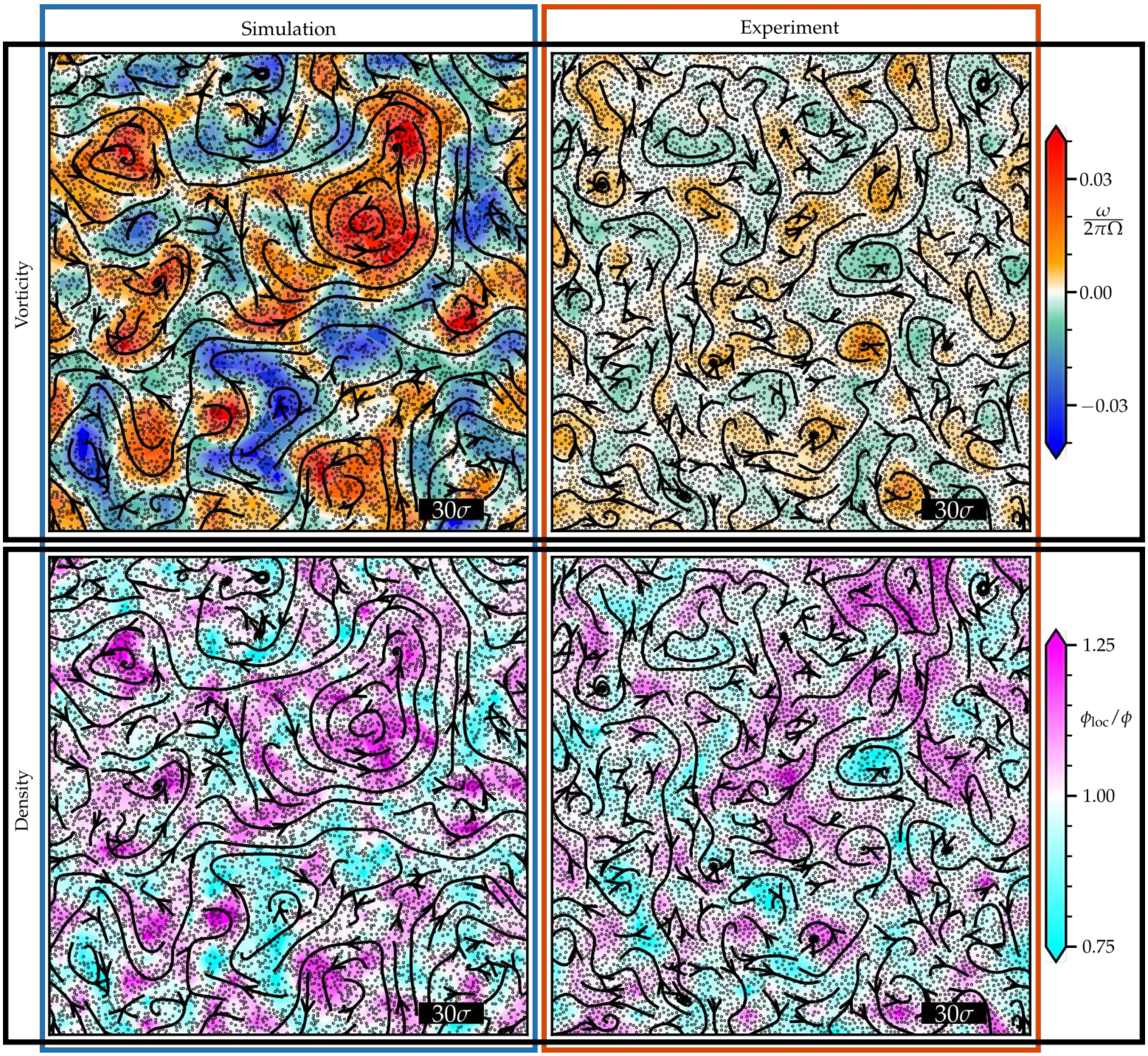

Figure 3: Vorticity and density fields. *Coarse-grained vorticity and local packing fraction fields of the rotor dynamics on a 2D square grid of binning length $l_0 = 10\sigma$ for simulation and experiment. In each column, the same system configuration has been used to generate the respective fields. Superimposed streamlines and rotor positions are displayed. The packing fraction used in experiments, simulations is $\phi = 0.144$, $\phi = 0.14$, respectively. The simulations have been performed in a square simulation box of length $L = 300\sigma$ with periodic boundaries.*

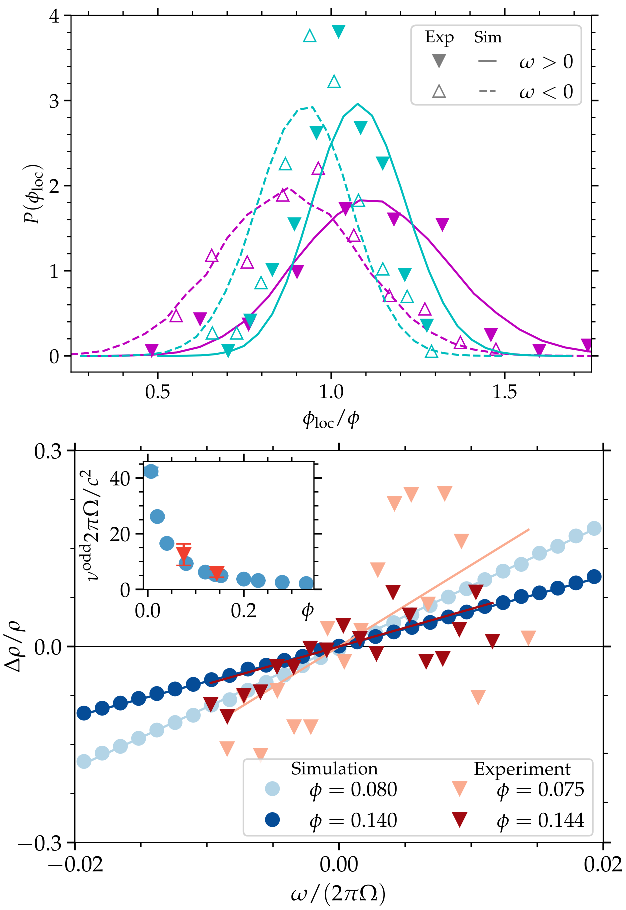

Figure 4: Vorticity-density correlations. a. *Normalised probability distribution of the local packing fraction ϕ_{loc} of the areas with positive vorticity (solid lines and solid symbols) and negative vorticity (dashed lines and open symbols). Lines correspond to simulation results and symbols to experimental ones. Results for lower volume fraction are shown in magenta (experiments $\phi = 0.075$ and simulations $\phi = 0.08$). Higher volume fraction results are shown in cyan (experiments $\phi = 0.144$ and simulations $\phi = 0.14$).* **b.** *Normalized variation of the local rotor mass density ρ as a function of the local vorticity ω. The lines indicate least-squares fits according to Eq. (1) with which ν^{odd} can be determined. The inset shows the estimates for the normalized odd viscosity as a function of the density for experiments (red symbols) and simulations (blue symbols).*

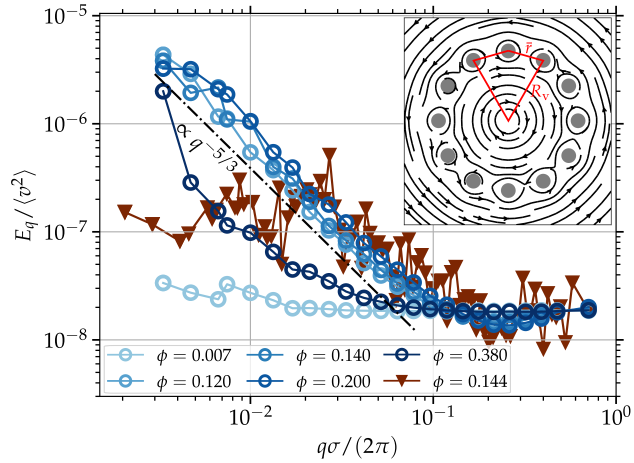

Figure 5: Energy spectra of the colloid dynamics. *Energy spectra obtained from the power-spectral-density of the rotor dynamics as in equation (9) divided by the mean-square velocity. Blue circles depict simulation data whereas red triangles denote experimental data. The experimental data is multiplied by a constant factor to match the high-q simulation values. The minimum and maximum wave numbers are $q_{\min}\sigma/(2\pi) = 3 \times 10^{-3}$ and $q_{\max}\sigma/(2\pi) = 7 \times 10^{-1}$. Inset: Averaged flow field in a simplified vortex, rotors arranged in a circle of radius R_v, with a fixed separation $\bar{r}$ between nearest neighbors.*

ing density. This decrease of ν^{odd} can also be observed in the larger separation of the maxima for lower densities in Fig. 4a. To the best of our knowledge, the odd viscosity was only quantified before in few very different systems, such as the so-called edge-pumping effect[24] in experiments, via the power spectra of the surface waves, measuring deformation of a flexible boundary, or as for a system of granular rotors, in simulations, measuring the normal stresses.[34]

(iv) Active turbulence. The colloid trajectories in Figs. 2**g-i** and the vorticity-density fields in Fig. 3 show the simultaneous presence of eddies of different sizes, which is clearly reminiscent of turbulence.[47] To provide a quantification of the turbulent dynamics, we investigate the rotor velocity field $\boldsymbol{v}(\boldsymbol{r})$ and its corresponding energy spectra E_q as a function of the wave vector q, defined in Eq.(10), see Fig. 5. Energy is injected in the system on the rotor size scale which determines a limiting maximum wave vector $q_{\max} \simeq 2\pi/\sigma$. Since the colloids only propel when nearby rotors break local symmetry, energy propagates because of the hydrodynamic forces, and is then transported to larger scales following self-similar dynamics along an inverse energy cascade. On the other hand, the vortex size has a maximum limit given by the system size, such that the minimum possible wave vector is $q_{\min} \simeq 2\pi/(L/2)$. In the limit $\phi \to 0$, the amount of cooperative motion is almost negligible and the colloids move like passive Brownian particles, such that the energy spectrum in Fig. 5 is almost white, *i.e.*, it practically does not display any dependence with the wave vector q. For intermediate ϕ, vortices of all sizes are taking part in the dynamics. The energy spectrum then follows a power-law decay $q^{-5/3}$. Approaching $q_{\max}$, the energy distribution deviates from the power-law and approaches a constant, which is related to the particle size. Simulations show the presence of very big vortices in Fig. 3, and the power law decay in Fig. 4 is valid almost up to $q_{\min}$. Experiments in Fig. 3 show that the maximum size of vortices is clearly smaller than the system size, and the power law decay is valid in a smaller range, namely until $q_1\sigma/(2\pi) \gtrsim 0.02$. This is due to the dissipation of energy through the substrate friction, which truncates the energy cascade. This is similar to 2D classical turbulence where the inverse cascade is truncated at $l_{\gamma_{\text{subs}}} \simeq \rho v_0(\phi)/\gamma_{\text{subs}}$, with a linear substrate friction density γ_{subs}.[48] From the value q_1, the maximum experimental vortex size can be estimated to be 50σ, which is consistent with the vortices in Fig. 4, and implies $\gamma_{\rm subs} = 7.63\,\mathrm{kg\,m^{-2}\,s^{-1}}$ Finally, at very high densities, steric interactions suppress rotor motion, and the free formation of vortices, such that it becomes increasingly difficult to measure the energy spectra. In contrast to bacterial turbulence, there is no dominant vortex scale that is introduced by the interplay of hydrodynamics, alignment interactions, activity, and rotational noise.[31,32]

To get a more intuitive insight on the self-similar behavior of the system, we consider a simplified picture of a vortex formed by a few rotors with fixed positions in a circle of radius $R_{\rm v}$, as shown in the inset of Fig. 5. If we approximate the drag on each rotor induced by the flow of its neighbours, the only a contribution remaining is, due to symmetry, tangential to the circular trajectory. This is the reason for the emergence of the circular arrangements, independent on their size, which are then perturbed by the presence of collisions, compressibility effects, and thermal fluctuations.

II. Summary

We have shown that rotating micrometer-sized particles are an interesting model system of chiral active matter, where the emergence of turbulence and odd viscosity can be simultaneously observed, as demonstrated here in experiments and simulations. While different types of rotating colloids are known to convert rotational into translational energy in symmetry-breaking situations, such as in the presence of confinement,[24,37] investigations of this effect in bulk were fragmentary, and the precise measurement of odd viscosity effects in low-Reynolds-number soft-matter systems was elusive until now.[12,13,41,49] Simulations and experiments are to a large degree in agreement, showing very similar behavior and dependence on system variables. Individual rotors behave similarly as active Brownian particles with their propulsion and rotational diffusion dependent on the configuration of neighbouring rotors. Translational velocity and rotational charateristic time can be measured and satisfactorily compared with an analytical prediction, for all the range of available concentrations. We furthermore present an effective method that allows the quantitative measurement of the bulk odd viscosity, shown here for experiments and simulations, and of use for a wide range of systems, such as roller liquids,[17,49] chiral granular gases,[50] or colloidal Janus asymmetric rotors[51,52]

Active turbulence in rotor materials is due to long-ranged hydrodynamic interactions and not due to the inherent particle properties: it can therefore be regarded as a new subclass of active turbulence in which the existence of a dominant vortex scale between lower and upper cutoff is lacking, a key feature of bacterial turbulence.[31] The appearance of both odd viscosity and active turbulence has its origin in the mechanism that converts rotational into translational energy. We expect these two concepts to be useful for various related hydrodynamic rotor systems of biological relevance, such as rotating membrane macromolecules, algae, or sperm, and also for the design of microrobots, and microrobots assemblies.[19,20,53,54]

III. Methods

Experimental setup. Silica rods with a magnetic head (Fe_3O_4) are used. The ferromagnetic material is grown on the Janus rods to impose a permanent magnetic dipole moment perpendicular to the rod long axis.[55] Directional growth of silica from nanoparticle encapsulated microemulsions droplets[56,57] is employed, followed by seeded growth of silica layers, which is a modification of the synthesis protocol of bare silica rods,[58] the Stober process. A scanning electron microscopy (SEM) image of these match-stick-like magnetic silica Janus rods is shown in Fig. 6a, where the inset shows a transmission electron microscopy (TEM) image highlighting the doping of magnetic nanoparticles at the head. This resulted in slightly tapered colloidal rods of $3.5 \pm 0.3\mu m$ in length, and a head and a tail of diameters of $0.77 \pm 0.08\mu m$ and $0.61 \pm 0.05\mu m$ respectively, measured from SEM images of approximately 70 particles. The ζ-potential of these particles are ~ -65 mV. Each rod possesses a permanent magnetic dipole moment in the end approximately perpendicular to its long axis. These particles were then suspended in deionized water (Millipore, 18.2 MΩ) and loaded into a custom sample chamber built by gluing a teflon cylinder (internal dimension: 1 cm; outer dimension: 2 cm; height: 1 cm) onto a piece of coverslip. The chamber was cleaned with isopropyl alcohol and DI water thoroughly before dried with nitrogen gas. The sample was allowed to rest on a microscope stage for 10 min until all the particles sediment to the bottom. A rotating magnetic field of 150 Gauss at constant angular velocity was applied by a pair of Helmholtz coils. All experiments were conducted at room temperature on an inverted light microscope (Olympus IX73) equipped with a 60× oil-immersion lens (NA of 1.42) and the images were captured by a Ximea color camera (MQ042Cg-CM). The centroids of rotors were determined by a standard Matlab routine.[59]

The magnetic field is generated by two pairs of orthogonally placed Helmholtz coils hosted on a home-built microscope stage, Fig. 6b. Under a slowly rotating magnetic field ($B = 150$ Gauss), the rod lays flat on the substrate due to gravity, with long axis aligned perpendicular to the applied field, Figure 6c. As a rotating magnetic field is applied between a certain range of frequency, typically $2 - 20Hz$, the rod stands up against gravity and rotates synchronously with the applied field, Fig. 6c, which we therefore term a rotor. In this study, we primarily focus on a rotating frequency of 10 Hz. We first examine the translational motion of a single rotor or a dilute suspension of rotors when they are far apart by measuring the mean squared displacements (MSD, $\langle r^2 \rangle$), which grows linearly with time, Fig. 6d, allowing the determination of the translational diffusion coefficient D. Typical trajectories are shown in the inset of Fig. 6d.

Simulation method. The employed numerical method, multiparticle collision dynamics, is a mesoscopic simulation technique to simulate fluids that does not rely on the microscopic degrees of freedom, and thus is not in need for calculating all the interactions between the solvent particles. The method includes hydrodynamic interactions and thermal fluctuations. Provided that suitable parameters are employed, the correct low-Reynolds number behaviour is reproduced.[60] The algorithm basically consists of two alternating steps. In the streaming step, the positions of the fluid particles are ballistically updated, *i.e.*, $\boldsymbol{r}_i(t+h) = \boldsymbol{r}_i(t) + \boldsymbol{v}_i(t)h$. The second step is the collision step, in which the fluid particles are sorted into square collision boxes of length $a = \sigma/6$ and exchange momentum with all particles in a given collision box according to a certain protocol. The collision routine we employ has already been introduced in reference.[61] It builds on the basic collision routine in which each fluid particle's relative velocity is rotated by an angle of $\pm\pi/2$ with respect to the centre of mass velocity in a collision box, with equal probability. When studying rotating objects, and to avoid the occurrence of unphysical torques in the fluid, angular momentum conservation is necessary. We employ a variant of the collision routine that conserves linear and angular momentum[62] but not energy. The colloids rotation constitutes a persistent input of energy in

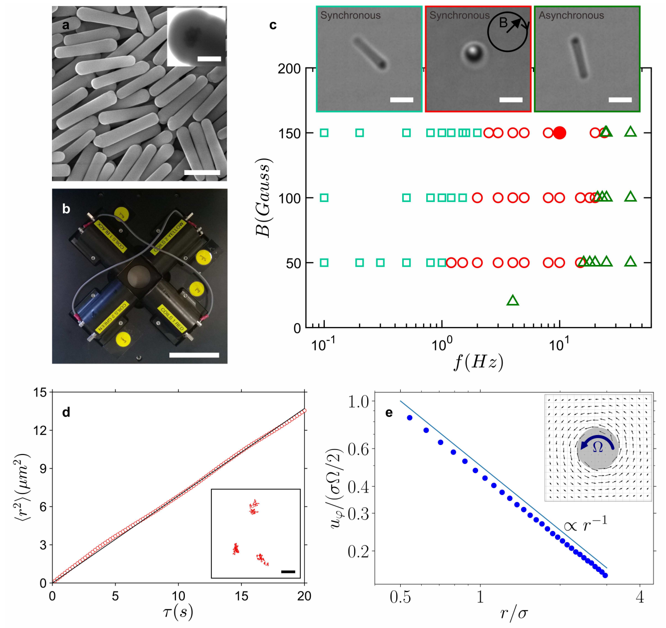

Figure 6: Experimental system and dynamics of single rotors. a. An SEM image of ferromagnetic Janus rods; the inset is a transmission electron microscopy image of the magnetic head of a rod; **b.** Experimental setup with two-pairs of orthogonally placed Helmholtz coils for generating a rotating magnetic field; **c.** State diagram of a single rod under a rotating magnetic field as a function of the frequency and the field strength. Insets show images of rods corresponding to the three dynamic states observed, horizontal rod rotating synchronously (light green squares), standing rod rotating synchronously (red circles), and horizontal rod rotating asynchronously (dark green triangles) with applied dynamic magnetic field. Most of experiments in the later work are conducted at a dynamic magnetic field of 10Hz and 150$Gauss$ (red bullet); Scalebars are 2μm in a, c, d, 10 cm in b, and 200 nm in the inset of a. **d.** Experimentally measured mean squared displacement of a single rotor (red circles) and its fit to $\langle r^2 \rangle = 4D\tau$, with $D = 0.171 \pm 0.001 \mu\text{m}^2/\text{s}$; Inset shows typical trajectories of rotors. **e.** Averaged fluid velocity $u_\varphi(r)$ in an axial direction as a function of distance from the colloid centre. Symbols are simulation results and the solid line corresponds to the analytical prediction, $u_\varphi(r) = \sigma^2\pi\Omega/(2r)$. Inset: Simulated 2D fluid averaged velocity field around a single rotor.

the system, which is compensated by considering a thermostat in each time step to all collision boxes individually,[63] becoming also a guarantee of a constant system temperature k_BT. For the fluid, we employ an average number of particles per collision cell $n = 10$ and take the collision time, *i.e.*, the time between two collisions, as $h = 0.02a\sqrt{m/(k_BT)}$, yielding a viscosity of $\eta = 17.9\sqrt{mk_BT}/a$, according to reference.[62]

The rotors are modelled as impenetrable moving and rotating no-slip boundaries that exchange linear and angular momentum with the fluid in the streaming step and in the collision step, by introducing virtual particles.[36,37] From the mean squared displacement in Figure 6d, the diffusion coefficient in the dilute regime can be determined to be $D = 3.73 \times 10^{-4}\sigma^2/(a\sqrt{m/(k_BT)})$. In the concentrated regime, rotors sterically interact with each other via a purely repulsive Lennard-Jones potential,

$$\mathcal{U}(r_{ij}) = \begin{cases} 4\varepsilon\left[\left(\frac{a}{r_{ij}-\sigma}\right)^{12} - \left(\frac{a}{r_{ij}-\sigma}\right)^{6}\right] + \varepsilon, & \text{for } r_{ij} \le \sigma + 2^{1/6}a \\ 0, & \text{else} \end{cases} \quad (2)$$

The rotors are therefore simulated as 2D impenetrable discs of diameter σ, and always roughly one collision box of fluid is between two rotors to ensure proper hydrodynamic coupling. Thus, after the momentum exchange between colloid and fluid, the positions of the rotors are updated according to a molecular dynamics scheme. The mass density of the colloids' material and the fluid mass density are taken to be the same. The angular velocity Ω of the colloids is fixed to $\Omega_0 = 0.01857/(a\sqrt{m/(k_BT)})$, if not otherwise stated. The interactions of the fluid particles with the colloid surface generates a co-rotation of the fluid with a velocity decaying in the azimuthal direction, as shown in the inset of Fig. 6e. The radial velocity profile quantitatively agrees with the measurements of the simulated flow, as shown in Fig. 6e. For the calculation of the packing fraction, we consider the hard cores of the rotors, that cannot be occupied by fluid, *i.e.*, an ensemble of N rotors in a square simulation box of length L has a packing fraction of $\phi = N\pi(\sigma/2)^2/L^2$. Simulations are performed in a square simulation box with periodic boundary conditions, with a box length $L = 300\sigma$ unless otherwise stated.

Simulation code was developed in CUDA C/C++, NVIDIA A100 GPUs in the JUWELS supercomputer and is typically used to simulate 30×10^6 solvent particles and up to 70,000 rotors.

Dipolar magnetic interactions. Provided the use of magnetic colloids, we experimentally quantify pair interactions parallel to the line of centres by estimating the effective pair potential as a function of radial distance,[64] $U(r) = -k_BT\log g(r)$. Results are shown in Fig. 7 for a dilute suspension of rotors for three values of the magnetic rotating frequency. At the lower frequency, the rotors only display repulsive interactions, while for increasing frequencies, a weak short-range attraction on the order of $0.2k_BT$ emerges. This proves that dipolar magnetic interactions between rotors are negligible in experiments, since they should be noticeable and decrease in intensity with frequency. The measurements of $F_\parallel$ in *ad hoc* simulations, corresponding to Fig. 1g, are shown in the inset of Fig. 7 to be attractive, but much smaller than the thermal noise, than $F_\perp$, and of shorter range. These measurements confirm that the dynamic behavior of the ferromagnetic rotors is dominated by hydrodynamic interactions, and that these are properly accounted for in the simulations.

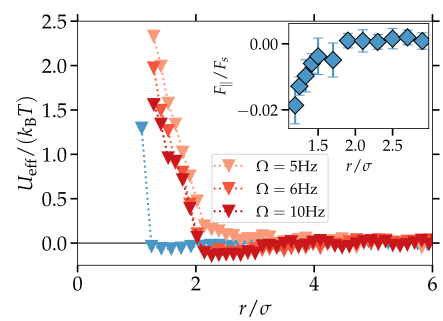

Figure 7: Effective pair potential. Estimated from the radial distribution function as $U(r) = -k_BT\log g(r)$ at density $\phi = 0.007$ for simulations (in blue) and $\phi = 0.0002$ for experiments (in red) at three input spin frequency values, showing the absence of significant dipolar magnetic interactions. Inset: Forces parallel to the line connecting the two rotors as measured in simulations.

Dimensionless numbers. The comparison between experiments and simulations is done via dimensionless quantities. Although single rotors cannot be considered as self-propelled particles, the magnetic activation can be quantified with the velocity at the colloid surface such that we consider the system Péclet number as $\text{Pe} = \Omega R^2/D$ and the Reynolds number $\text{Re} = \Omega\sigma^2/(2\nu)$ with σ the particle diameter, D the colloid diffusion coefficient, and ν the fluid kinematic viscosity. With specified default values, in experiments we are working with $\text{Re} \approx 10^{-5}$ and $\text{Pe} \simeq 38$, for which the rod-head diameter has been considered. Meanwhile in simulations, $\text{Re} \simeq 0.09$ and $\text{Pe} \simeq 20$, respectively. Clearly, the input parameters do not perfectly match, but these dimensionless numbers ensure that both simulations and experiments, are performed in the regime of low Reynolds and large Péclet numbers, where the same physical behavior is to be expected.

Vortex dynamics in Stokes flow with odd viscosity. The Stokes equation of a chiral active fluid describes the time evolution of the flow velocity $\boldsymbol{u}$, in terms of its density ρ, pressure p, kinematic viscosity

ν, vorticity $\omega = \varepsilon_{\alpha\beta}\partial_\alpha u_\beta$ (where the Einstein notation is considered, and $\varepsilon_{\alpha\beta}$ is the Levi-Civita sysmbol), and importantly also by the odd kinematic viscosity ν^{odd}, which is proportional to the field of intrinsic rotation $\widetilde{\Omega} = \Omega\langle\sum_i \delta(\boldsymbol{r}-\boldsymbol{r}_i)\rangle$, as[22,46]

$$\rho\partial_t u_\alpha = -\partial_\alpha\left(p - \rho\nu^{\text{odd}}\omega\right) + \rho\nu\partial_\beta\partial_\beta u_\alpha\,, \tag{3}$$

Taking the curl of Eq. (3) leads to the vorticity diffusion equation

$$\partial_t\omega = \nu\partial_\beta\partial_\beta\omega\,. \tag{4}$$

which can be solved with Fourier transform methods. The initial condition of a line or puntual vortex $\omega(\boldsymbol{r}, t=0) = \Lambda\delta(\boldsymbol{r})$ which later diffuses due to viscosity can be considered, in order to account for the internal vortex dynamics of the system together with Eq. (4). The solution is then,

$$\omega(\boldsymbol{r}, t) = \frac{\Lambda}{4\pi\nu t}e^{-\frac{r^2}{4\nu t}}\,. \tag{5}$$

Integrating this expression results in an expression for the velocity profile in polar coordinates when incompressibility is ensured, $\partial_\alpha u_\alpha = 0$, leading to

$$u_\varphi(r,t) = \frac{\Lambda}{2\pi r}\left(1 - e^{-\frac{r^2}{4\nu t}}\right) \tag{6}$$

and $u_r = 0$. These expressions of the flow field together with Eq. (3) yields to the following relation in the radial direction

$$0 = \partial_r\left(p - \rho\nu^{\text{odd}}\omega\right)\,, \tag{7}$$

and thus $p - p_0 = \rho\nu^{\text{odd}}\omega$, with $p_0 \equiv p(r\to\infty)$. This means, that the pressure compensates the antisymmetric stress stemming from odd viscosity in order to satisfy incompressibility. If small changes in density due to finite compressibility are now considered,[47] and assuming $\Delta p = c^2\Delta\rho$ with $\Delta p = p - p_0$ and $\Delta\rho = \rho - \rho_0$, we obtain the expression for the density accumulation in Eq. (1), also employed for the measurements in Fig. 4b.

Note that Eq. (3) might include two additional terms, one accounting for rotational friction among the rotors and the other for the friction between the rotor fluid and the substrate. The first of which is proportional to the rotational kinetic viscosity ν_{R} and takes the form $\varepsilon_{\alpha\beta}\partial_\beta\rho\nu_{\text{R}}(2\widetilde{\Omega} - \omega)$, and is the coarse-grained version of the hydrodynamic coupling of intrinsic rotation and translational degrees of freedom. The second term is proportional to the substrate friction coefficient γ_{subs} and takes the form $-\gamma_{\text{subs}}u_\alpha$. However, both terms do not alter the result in Eq. (1), if incompressibility to arrive at Eq. (7), and $\widetilde{\Omega} = \text{const.}$, *i.e.*, a homogeneous rotor density, is assumed.

Turbulence analysis. To analyse the turbulent dynamics of the system, we investigate the velocity field $\boldsymbol{v}(\boldsymbol{r})$ and its corresponding energy spectra E_q. The formal definition of E_q is

$$E_{\text{kin}} = \frac{1}{2}\langle v^2\rangle = \int_0^\infty \mathrm{d}q\, E_q\,, \tag{8}$$

with reciprocal space vector $\boldsymbol{q}$ and $q \equiv |\boldsymbol{q}|$. Using the Wiener-Khintchin theorem to express the correlation function $\langle v^2\rangle$ in terms of reciprocal variables and assuming isotropy, we can write

$$E_{\text{kin}} = \frac{1}{4\pi}\int_0^\infty \mathrm{d}q\, q\, \langle\hat{\boldsymbol{v}}\cdot\hat{\boldsymbol{v}}^*\rangle_{\boldsymbol{q}}\,, \tag{9}$$

where $\langle\hat{\boldsymbol{v}}\cdot\hat{\boldsymbol{v}}^*\rangle_{\boldsymbol{q}}$ is the two-dimensional Fourier transform of the velocity correlation function. The integral in Eq. (9) goes over values of $\langle\hat{\boldsymbol{v}}\cdot\hat{\boldsymbol{v}}^*\rangle_{\boldsymbol{q}}$ in radially symmetric shells in q-space. In a discretised version of Eq. (9), the integral is then evaluated as a sum over the discretised values in equal-q shells, *i.e.*,

$$E_q = \frac{1}{8\pi\Delta q}\sum_{q-\Delta q<k<q+\Delta q}\langle\hat{\boldsymbol{v}}\cdot\hat{\boldsymbol{v}}^*\rangle_{\boldsymbol{k}}\,. \tag{10}$$

Calculation of coarse-grained values. Experiments and simulations provide configurations at different times where the rotors positions are well defined. Additionally, in simulations we obtain the instantaneous rotor velocities. In order to obtain the necessary density, velocity, and vorticity fields required in our study a coarse-grained procedure is applied. Density $\rho(r)$ is obtained by averaging the rotors positions in a grid with a bin size that might vary, but typically $(10\sigma)^2$. The bin size should be at least a few colloid diameters in order to identify coarse grain effects, but not much larger, since the structure of small vortices would already be averaged out. Coarse-grained velocities are obtained with two configurations at close times, $\boldsymbol{v}(\boldsymbol{r},t) = (\boldsymbol{r}(t+\Delta t) - \boldsymbol{r}(t))/\Delta t$, with the time interval has been chosen such that $\Omega\Delta t \leq 2$, where in simulations higher resolution is possible, which is necessary at high densities due to frequent inter-rotor collisions. The velocity, and thus vorticity fields are then obtained by averaging the rotor velocities in each bin. For the calculation of the energy spectra, we employ a bin size of σ^2 in order to obtain highest resolution in q-space.

Data availability

The data that support the findings of this study are available from the corresponding authors upon reasonable request.

Code availability

The custom code for the simulations on GPUs is available from the corresponding authors upon reasonable request.

Author contributions

J.M., M.R, and G.G. designed the numerical approach, J.M. and C.A.R.M. wrote the simulation code, and J.M. conducted the numerical simulations. Y.G. and D.G.A.L.A. designed the experimental setup, and Y.G. performed the experiments. J.M., Y.G., and M.R. analyzed the data and wrote the original draft. J.M., Y.G., D.G.A.L.A, G.G., and M.R. discussed the data and finalized the manuscript. All authors approved the final manuscript.

Acknowledgements

J.M., C.A.R.M., and M.R. gratefully acknowledge the Gauss Centre for Supercomputing e.V. (www.gauss-centre.eu) for funding this project by providing computing time through the John von Neumann Institute for Computing (NIC) on the GCS Supercomputer JUWELS at Jülich Supercomputing Centre (JSC) and the Helmholtz Data Federation (HDF) for funding this work by providing services and computing time on the HDF Cloud cluster at the Jülich Supercomputing Centre (JSC). Y.G. acknowledges funding support from National Natural Science Foundation of China (Project no.11774237) and Natural Science Foundation of Guangdong Province (no. 2022A1515011800).

References

[1] Elgeti, J., Winkler, R. G. & Gompper, G. Physics of microswimmers—single particle motion and collective behavior: A review. *Rep. Prog. Phys.* **78**, 056601 (2015).

[2] Gompper, G. *et al.* The 2020 motile active matter roadmap. *J. Phys. Condens. Matter* **32**, 193001 (2020).

[3] Cavagna, A. & Giardina, I. Bird flocks as condensed matter. *Annu. Rev. Condens. Matter Phys.* **5**, 183–207 (2014).

[4] Helbing, D. Traffic and related self-driven many-particle systems. *Rev. Mod. Phys.* **73**, 1067 (2001).

[5] Dombrowski, C., Cisneros, L., Chatkaew, S., Goldstein, R. E. & Kessler, J. O. Self-concentration and large-scale coherence in bacterial dynamics. *Phys. Rev. Lett.* **93**, 098103 (2004).

[6] Zhang, H., Be'Er, A., Smith, R. S., Florin, E.-L. & Swinney, H. L. Swarming dynamics in bacterial colonies. *EPL* **87**, 48011 (2009).

[7] Colberg, P. H. & Kapral, R. Many-body dynamics of chemically propelled nanomotors. *J. Chem. Phys.* **147**, 064910 (2017).

[8] Wagner, M., Roca-Bonet, S. & Ripoll, M. Collective behavior of thermophoretic dimeric active colloids in three-dimensional bulk. *Eur. Phys. J. E* **44**, 1–11 (2021).

[9] Medina-Sánchez, M., Schwarz, L., Meyer, A. K., Hebenstreit, F. & Schmidt, O. G. Cellular cargo delivery: Toward assisted fertilization by sperm-carrying micromotors. *Nano Lett.* **16**, 555–561 (2016).

[10] Langer, R. New methods of drug delivery. *Science* **249**, 1527–1533 (1990).

[11] Fernandez-Rodriguez, M. A. *et al.* Feedback-controlled active brownian colloids with space-dependent rotational dynamics. *Nat. Commun.* **11**, 4223 (2020).

[12] Han, K. *et al.* Reconfigurable structure and tunable transport in synchronized active spinner materials. *Sci. Adv.* **6**, eaaz8535 (2020).

[13] Kokot, G. *et al.* Active turbulence in a gas of self-assembled spinners. *Proc. Natl. Acad. Sci.* **114**, 12870–12875 (2017).

[14] Grzybowski, B. A., Stone, H. A. & Whitesides, G. M. Dynamic self-assembly of magnetized, millimetre-sized objects rotating at a liquid–air interface. *Nature* **405**, 1033–1036 (2000).

[15] Grzybowski, B. A., Jiang, X., Stone, H. A. & Whitesides, G. M. Dynamic, self-assembled aggregates of magnetized, millimeter-sized objects rotating at the liquid-air interface: Macroscopic, two-dimensional classical artificial atoms and molecules. *Phys. Rev. E* **64**, 011603 (2001).

[16] Kavčič, B., Babič, D., Osterman, N., Podobnik, B. & Poberaj, I. Magnetically actuated microrotors with individual pumping speed and direction control. *Appl. Phys. Lett.* **95**, 023504 (2009).

[17] Kokot, G. & Snezhko, A. Manipulation of emergent vortices in swarms of magnetic rollers. *Nat. Commun.* **9**, 2344 (2018).

[18] Goto, Y. & Tanaka, H. Purely hydrodynamic ordering of rotating disks at a finite reynolds number. *Nat. Commun.* **6**, 5994 (2015).

[19] Lenz, P., Joanny, J.-F., Jülicher, F. & Prost, J. Membranes with rotating motors. *Phys. Rev. Lett.* **91**, 108104 (2003).

[20] Drescher, K. *et al.* Dancing volvox: hydrodynamic bound states of swimming algae. *Phys. Rev. Lett.* **102**, 168101 (2009).

[21] Abanov, A. Model oddity. *Nat. Phys.* **15**, 1109–1110 (2019).

[22] Banerjee, D., Souslov, A., Abanov, A. G. & Vitelli, V. Odd viscosity in chiral active fluids. *Nat. Commun.* **8**, 1573 (2017).

[23] Lapa, M. F. & Hughes, T. L. Swimming at low reynolds number in fluids with odd, or hall, viscosity. *Phys. Rev. E* **89**, 043019 (2014).

[24] Soni, V. *et al.* The odd free surface flows of a colloidal chiral fluid. *Nat. Phys.* **15**, 1188–1194 (2019).

[25] Dunkel, J. *et al.* Fluid dynamics of bacterial turbulence. *Phys. Rev. Lett.* **110**, 228102 (2013).

[26] Wensink, H. H. *et al.* Meso-scale turbulence in living fluids. *Proc. Natl. Acad. Sci.* **109**, 14308–14313 (2012).

[27] Creppy, A., Praud, O., Druart, X., Kohnke, P. L. & Plouraboué, F. Turbulence of swarming sperm. *Phys. Rev. E* **92**, 032722 (2015).

[28] Giomi, L. Geometry and topology of turbulence in active nematics. *Phys. Rev. X* **5**, 031003 (2015).

[29] Doostmohammadi, A., Shendruk, T. N., Thijssen, K. & Yeomans, J. M. Onset of meso-scale turbulence in active nematics. *Nat. commun.* **8**, 15326 (2017).

[30] Doostmohammadi, A., Ignés-Mullol, J., Yeomans, J. M. & Sagués, F. Active nematics. *Nat. commun.* **9**, 3246 (2018).

[31] Qi, K., Westphal, E., Gompper, G. & Winkler, R. G. Emergence of active turbulence in microswimmer suspensions due to active hydrodynamic stress and volume exclusion. *Commun. Phys.* **5**, 49 (2022).

[32] Heidenreich, S., Dunkel, J., Klapp, S. H. & Bär, M. Hydrodynamic length-scale selection in microswimmer suspensions. *Phys. Rev. E* **94**, 020601 (2016).

[33] Reeves, C. J., Aranson, I. S. & Vlahovska, P. M. Emergence of lanes and turbulent-like motion in active spinner fluid. *Commun. Phys.* **4**, 92 (2021).

[34] Yang, Q. *et al.* Topologically protected transport of cargo in a chiral active fluid aided by odd-viscosity-enhanced depletion interactions. *Phys. Rev. Lett.* **126**, 198001 (2021).

[35] Malevanets, A. & Kapral, R. Mesoscopic model for solvent dynamics. *J. Chem. Phys.* **110**, 8605–8613 (1999).

[36] Götze, I. O. & Gompper, G. Dynamic self-assembly and directed flow of rotating colloids in microchannels. *Phys. Rev. E* **84**, 031404 (2011).

[37] Götze, I. O. & Gompper, G. Flow generation by rotating colloids in planar microchannels. *EPL* **92**, 64003 (2011).

[38] Ueda, Y., Sellier, A., Kida, T. & Nakanishi, M. On the low-reynolds-number flow about two rotating circular cylinders. *J. Fluid Mech.* **495**, 255–281 (2003).

[39] Howse, J. R. *et al.* Self-motile colloidal particles: from directed propulsion to random walk. *Phys. Rev. Lett.* **99**, 048102 (2007).

[40] Winkler, R. G., Wysocki, A. & Gompper, G. Virial pressure in systems of spherical active brownian particles. *Soft Matter* **11**, 6680–6691 (2015).

[41] Llopis, I. & Pagonabarraga, I. Hydrodynamic regimes of active rotators at fluid interfaces. *Eur. Phys. J. E* **26**, 103–113 (2008).

[42] Einstein, A. Eine neue bestimmung der moleküldimensionen. *Ann. Phys.* **324**, 289–306 (1906).

[43] Stenhammar, J., Tiribocchi, A., Allen, R. J., Marenduzzo, D. & Cates, M. E. Continuum theory of phase separation kinetics for active brownian particles. *Phys. Rev. Lett.* **111**, 145702 (2013).

[44] Haines, B. M., Aranson, I. S., Berlyand, L. & Karpeev, D. A. Effective viscosity of dilute bacterial suspensions: a two-dimensional model. *Phys. Biol.* **5**, 046003 (2008).

[45] Krieger, I. M. & Dougherty, T. J. A mechanism for non-newtonian flow in suspensions of rigid spheres. *T. Soc. Rheol.* **3**, 137–152 (1959).

[46] Avron, J. Odd viscosity. *J. Stat. Phys.* **92**, 543–557 (1998).

[47] Landau, L. & Lifshitz, E. *Fluid mechanics*, vol. 6 of *Course of theoretical physics* (Pergamon press, 1987), 2nd edn.

[48] Boffetta, G. & Ecke, R. E. Two-dimensional turbulence. *Annu. Rev. Fluid Mech.* **44**, 427–451 (2012).

[49] Han, K., Glatz, A. & Snezhko, A. Emergence and dynamics of unconfined self-organised vortices in active magnetic roller liquids. *Soft Matter* **17**, 10536–10544 (2021).

[50] Tsai, J.-C., Ye, F., Rodriguez, J., Gollub, J. P. & Lubensky, T. A chiral granular gas. *Phys. Rev. Lett.* **94**, 214301 (2005).

[51] Löwen, H. Chirality in microswimmer motion: From circle swimmers to active turbulence. *Eur. Phys. J.: Spec. Top.* **225**, 2319–2331 (2016).

[52] Van Teeffelen, S. & Löwen, H. Dynamics of a brownian circle swimmer. *Phys. Rev. E* **78**, 020101 (2008).

[53] Riedel, I. H., Kruse, K. & Howard, J. A self-organized vortex array of hydrodynamically entrained sperm cells. *Science* **309**, 300–303 (2005).

[54] Palagi, S. & Fischer, P. Bioinspired microrobots. *Nat. Rev. Mater.* **3**, 113–124 (2018).

[55] Gao, Y., Balin, A. K., Dullens, R. P., Yeomans, J. M. & Aarts, D. G. Thermal analog of gimbal lock in a colloidal ferromagnetic janus rod. *Phys. Rev. Lett.* **115**, 248301 (2015).

[56] Gao, Y., Romano, F., Dullens, R. P., Doye, J. K. & Aarts, D. G. Directed self-assembly into low-density colloidal liquid crystal phases. *Phys. Rev. Mater.* **2**, 015601 (2018).

[57] Gao, Y., Dullens, R. P. & Aarts, D. G. Bulk synthesis of silver-head colloidal rodlike micromotors. *Soft Matter* **14**, 7119–7125 (2018).

[58] Kuijk, A., Van Blaaderen, A. & Imhof, A. Synthesis of monodisperse, rodlike silica colloids with tunable aspect ratio. *J. Am. Chem. Soc.* **133**, 2346–2349 (2011).

[59] Gao, Y. & Kilfoi, M. L. Accurate detection and complete tracking of large populations of features in three dimensions. *Opt. Express* **17**, 4685–4704 (2009).

[60] Ripoll, M., Mussawisade, K., Winkler, R. & Gompper, G. Dynamic regimes of fluids simulated by multiparticle-collision dynamics. *Phys. Rev. E* **72**, 016701 (2005).

[61] Theers, M., Westphal, E., Gompper, G. & Winkler, R. G. Modeling a spheroidal microswimmer and cooperative swimming in a narrow slit. *Soft Matter* **12**, 7372–7385 (2016).

[62] Noguchi, H. & Gompper, G. Transport coefficients of off-lattice mesoscale-hydrodynamics simulation techniques. *Phys. Rev. E* **78**, 016706 (2008).

[63] Huang, C.-C., Chatterji, A., Sutmann, G., Gompper, G. & Winkler, R. G. Cell-level canonical sampling by velocity scaling for multiparticle collision dynamics simulations. *J. Comput. Phys.* **229**, 168–177 (2010).

[64] Behrens, S. H. & Grier, D. G. Pair interaction of charged colloidal spheres near a charged wall. *Phys. Rev. E* **64**, 050401 (2001).

Supplementary Files

This is a list of supplementary files associated with this preprint. Click to download.

- M1tworotors.mov
- M2collectivedynamics1.mov
- M3collectivedynamics2.mov
- M4collectivedynamics3.mov
- M5bulkdynamics.mov